Circular Harmonic Decomposition Approach for Numerical Inversion of Circular Radon Transforms

Gaël Rigaud
ETIS-ENSEA/Univ.
Cergy-Pontoise/CNRS
95000 Cergy-Pontoise, France
gael.rigaud@ensea.fr

Maï K. Nguyen
ETIS-ENSEA/Univ.
Cergy-Pontoise/CNRS
95000 Cergy-Pontoise, France
mai.nguyen-verger@u-cergy.fr

Alfred K. Louis
Fachbereich Mathematik
Universität des Saarlandes
D-66041 Saarbrücken,
Germany
louis@num.uni-sb.de

ABSTRACT

Numerical inversions via circular harmonic decomposition for two classes of circular Radon transforms are established. The first class deals with the Radon transform (RT) defined on circular arcs having a chord of fixed length rotating around its middle point (CART) and the second is the RT defined on a set of circles passing through a fixed point of the plane (CRT). These circular Radon transforms arise from the modeling of different modalities in Compton scattering tomography (CST). Inversions via circular harmonic decomposition are used for image reconstructions in CST. Simulation results show the efficiency and interest of this inversion method in imaging science.

Keywords

Radon transforms (RT), Circular Radon transform (CRT), Circular-arc Radon transform (CART), image reconstruction, Circular Harmonic Decomposition (CHD), Compton scattering tomography (CST)

1. INTRODUCTION

Since the seminal work of J Radon [1], which finds numerous applications (Computed Tomography, Single Photon Emission Computed Tomography (SPECT) and Positron Emission Tomography (PET), etc.) many extensions of this integral transform have been widely discussed, in particular in the literature of imaging science. This is the case when results of measurements appear under the form of integrals of a physical quantity over lower dimensional manifolds. The relevant problem to solve is the recovery of the physical quantity of interest as a function in $\mathbb{R}^2$. The field of such problems is known in mathematics as integral geometry and in image processing as image reconstruction.

As the circle is the simplest curve in the plane next to the straight line, it becomes the natural object on which a new Radon transform can be defined. Circular Radon transforms along paths that are not on the zero sets of harmonic polynomials were proved to be invertible. Quinto [2] has discussed the case of all translations of a circle of fixed radius as well as circles centered on a circle. Finally Compton scattering tomography, a two-dimensional imaging process based on scattered radiation, has two modalities for which image formation is built on Radon transforms defined on a set of circles passing through a fixed point of the plane and on circular arcs having a chord of fixed length rotating around its middle point.

In image reconstruction all these modelings of physical phenomenon lead to an inversion of the established forward transform in order to reconstruct the original function. But generally the obtained inversion formula is not adapted for computation because of singularities. A regularization has to be applied and computational methods can be derived.

In this paper we describe two novel computational methods via circular harmonic decomposition (CHD) for circular Radon transforms. The CHD was introduced by Cormack [3, 4] and is very adapted to a polar approach of the studied forward transforms. Indeed Cormack has shown several properties of the circular harmonic components of the data for a given family of curves in the plane which lead to an inversion and to a regularization procedure. This way permits to fulfill the consistency criterion of the data and so to reduce the number of artifacts, which is not the case of the well-known "Filtered Back-Projection" algorithm. Our work is based on these two procedures and on a computational approach of Chapman and Cary [5] who have discussed an alternative algorithm to the "Filtered Back-Projection" algorithm for the inverse Radon transform. We first use the same algorithm in the case of a circular-arc Radon transform then we will establish a algorithm for the inverse circular Radon transform defined on a set of circles passing through a fixed point. Finally, we present numerical results of these two algorithms used in emerging CST and compare them with those obtained for conventional tomography modeled by the classical Radon transform and computed by the filtered backprojection algorithm in the first case and with the inversion formula established by S.J. Norton [6] in the second case.

2. COMPTON SCATTERING TOMOGRAPHIES BASED ON CIRCULAR RADON TRANSFORMS

In this part, we will present the working principles of two modalities in Compton scattering tomography and the associated Radon's problems. We will see how to model the physical phenomenon as an integral of the studied function on the corresponding curve and how to inverse these transforms.

2.1 Novel CST modality based on Circular-Arc Radon transform

Consider a two-dimensional object represented by a non-negative continuous function $f(\mathbf{M})$ with bounded support in $\mathbb{R}^2$. Fig. 1 shows how Compton scattering tomography works. An emitting point source **S** is placed at a distance $2p$ from a point detector **D**. We consider only the upper part of space. This is possible because an angle collimator is placed at **D**. The segment **SD** rotates around its middle **O** and its angular position is given by φ.

Emitted photons are scattered at site **M** and some of them are detected by the detector **D** at an energy E_ω. Therefore the detector can record scattered photons according to scattered energy which is related to the scattering angle ω by the Compton formula. Thus, for a fixed φ, to each energy E_ω corresponds a set of scattering sites on a circular arc $C(\varphi,\omega)$.

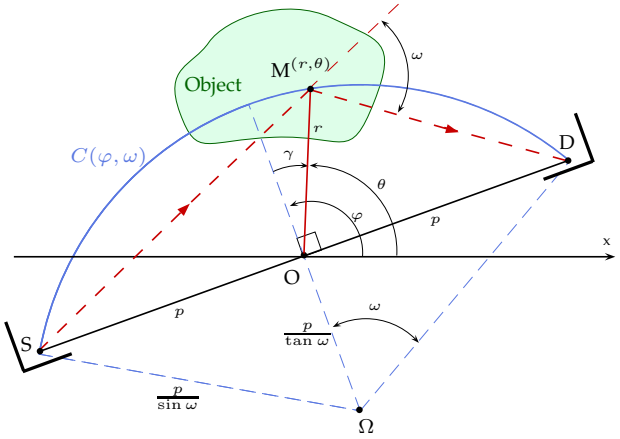

Figure 1: Principle of the new CST based on the CAR transform.

Finally the detected radiation flux density $g(\varphi,\omega)$ is proportional to the integral of the electron density $f(\mathbf{M})$ with $\mathbf{M} \in C(\varphi,\omega)$ which can be written as the Radon transform extended on the corresponding circular arcs $C(\varphi,\omega)$

$$\tilde{\mathcal{C}}^2 f(\varphi,\omega) = \int\limits_{(r,\theta)\in C(\varphi,\omega)} f(r,\theta)ds \tag{1}$$

where $\tilde{\mathcal{C}}^2$ is the circular-arc Radon transform (CART) established in (φ,ω)-space and ds is the elementary length of circular arc to be computed from the circular arc equation

$$r = p(\sqrt{1+\tau^2\cos^2\gamma} - \tau\cos\gamma)\ , \tag{2}$$

where $\tau = \cot\omega$ and $\gamma = \theta - \varphi$ and with $(\omega,\varphi) \in]0,\frac{\pi}{2}] \times [0,2\pi]$. Putting τ in equation (1), we obtain :

$$\mathcal{C}^2 f(\varphi,\tau) = \int_{-\frac{\pi}{2}}^{\frac{\pi}{2}} f(r(\gamma),\gamma+\varphi)\ r(\gamma)\ \frac{\sqrt{1+\tau^2}}{\sqrt{1+\tau^2\ \cos^2\gamma}} d\gamma\ . \tag{3}$$

where $\mathcal{C}^2$ is the circular-arc Radon transform (CART) established in (φ,τ)-space. Thus equation (3) is the image formation.

The inverse transform can be worked out using the Fourier angular components of f and $\mathcal{C}^2 f$:

$$\begin{cases} f(r,\theta) = \sum\limits_l f_l(r)e^{il\theta} \\ \quad \text{with} \\ f_l(r) = \dfrac{1}{2\pi}\displaystyle\int_0^{2\pi} f(r,\theta)e^{-il\theta}d\theta \end{cases}$$

and (4)

$$\begin{cases} \mathcal{C}^2 f(\varphi,\tau) = \sum\limits_l \mathcal{C}^2 f_l(\tau)e^{il\varphi} \\ \quad \text{with} \\ \mathcal{C}^2 f_l(\tau) = \dfrac{1}{2\pi}\displaystyle\int_0^{2\pi} \mathcal{C}^2 f(\varphi,\tau)e^{-il\varphi}d\varphi \end{cases}$$

Following [7] we give a new integral equation linking $\mathcal{C}^2 f_l(\tau)$ to $f_l(r)$, the circular components of $\mathcal{C}^2 f(\varphi,\tau)$ and $f(r,\theta)$. Since $\gamma = \theta - \varphi$ and accounting for the invariance of the integrand under $\gamma \longleftrightarrow -\gamma$, equation (3) takes the form

$$\mathcal{C}^2 f_l(\tau) = 2\int_0^{\frac{\pi}{2}} r(\gamma)\frac{\sqrt{1+\tau^2}}{\sqrt{1+\tau^2\ \cos^2(\gamma)}}\ f_l(\gamma)\ \cos(|l|\gamma)d\gamma\ . \tag{5}$$

The absolute value of l is due to the invariance : $f_{-l}(r) = f_l^*(r)$. Because of the equation of the circular arc (equation (2)), we can show that

$$d\gamma\frac{r(\cos\gamma)}{\sqrt{1+\tau^2\cos^2\gamma}} = \frac{dr}{\sqrt{\tau^2 - \frac{1}{4}\left(\frac{p}{r} - \frac{r}{p}\right)^2}}\ . \tag{6}$$

Now using this relationship between the differential elements, we change back to the r-variable equation (5) to obtain:

$$\frac{\tau\,\mathcal{C}^2 f_l(\tau)}{\sqrt{1+\tau^2}} = 2\int_{p(\sqrt{1+\tau^2}-\tau)}^{p} \frac{dr}{\sqrt{1-\frac{1}{4\tau^2}\left(\frac{p}{r}-\frac{r}{p}\right)^2}}\, f_l(r) \times \cos\left[|l|\cos^{-1}\left(\frac{1}{2\tau}\left(\frac{p}{r}-\frac{r}{p}\right)\right)\right] . \quad (7)$$

This new form is adapted to Cormack's inversion procedure [3]. In the term $\cosh(l\cosh^{-1}(h(r,\tau)))$, the function $h(r,\tau)$ is a product of functions of r and of τ, i.e $h(r,\tau) = h_1(r) \times h_2(\tau)$.

We can choose the following change of variables [7],

$$q = \frac{1}{\tau} = \tan\omega, \quad \text{and} \quad t^{-1} = \frac{1}{2}\left(\frac{p}{r}-\frac{r}{p}\right). \quad (8)$$

Then we apply the Cormack's procedure [3] to invert equation (7) and obtain the inverse transform of the CART through the circular harmonic decomposition :

$$f_l(r) = (-)\frac{2p(p^2+r^2)}{\pi(p^2-r^2)^2} \left[\frac{d}{dt}\int_t^\infty \frac{\cosh(|l|\ \cosh^{-1}(\frac{q}{t}))}{q\sqrt{(\frac{q}{t})^2-1}}\frac{\mathcal{C}^2 f_l(\frac{1}{q})}{\sqrt{1+q^2}}dq\right]_{t=\frac{2pr}{p^2-r^2}} . \quad (9)$$

An alternative form of this result can be obtained with a further change of variables in the integration. Equation (9) may be now recast as

$$f_l(r) = (-)\frac{2p(p^2+r^2)}{\pi(p^2-r^2)^2} \left[\int_t^\infty \frac{\cosh(|l|\ \cosh^{-1}(\frac{q}{t}))}{\sqrt{q^2-t^2}}\frac{d}{dq}\left(\frac{\mathcal{C}^2 f_l(\frac{1}{q})}{\sqrt{1+q^2}}\right)dq\right]_{t=\frac{2pr}{p^2-r^2}} . \quad (10)$$

Finally $f(r,\theta)$ is reconstructed through its Fourier expansion with the circular harmonic components $f_l(r)$. We have established the forward and inverse transforms in the case of this new Compton scattering tomography. In the next section, we will discuss how to use these transforms for numerical image reconstruction.

2.2 Norton's CST and Circular Radon transform

In 1994, S.J. Norton [6] worked out a CST modality which is based on a Radon transform on circles having a fixed common point. The working principle is given by Fig. 2. A point source **S** emits primary radiation towards an object defined by its electron density function $n_e(r,\theta)$, of which **M** is a scattering site (running point).

A point detector **D** moves along an Ox-axis and collects, at given energy E, scattered radiation from the object. The physics of Compton scattering demands that the registered radiation flux density g at site **D** is due to the contribution of all scattering sites **M** lying on an arc of circle from **S** to **D** subtending an angle $(\pi - \omega)$, where ω is the scattering angle corresponding to the outgoing energy E, as given by the Compton formula.

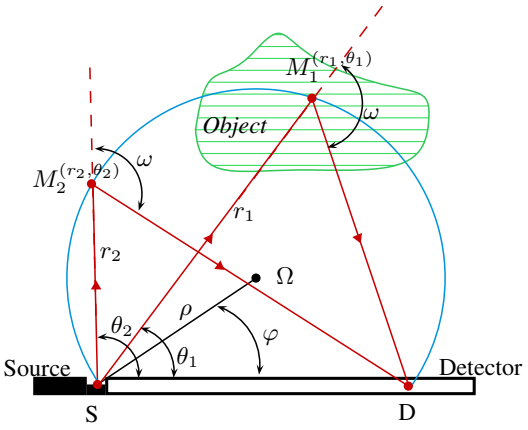

Figure 2: Principle of Norton's CST

Norton gave the expression of the projections g as :

$$g(\rho,\varphi) = \int_0^\pi d\theta \int_0^\infty dr\ \rho\, n_e(r,\theta)\, w(r,\theta;\rho,\varphi) \times \delta\left[r - 2\rho\cos(\theta-\varphi)\right] \quad (11)$$

where $\delta(.)$ is the 1-D Dirac delta function and $w(.)$ is defined by:

$$w(r,\theta;\rho,\varphi) = \frac{a\ r\ s(\theta)\ P(\varphi)}{4\pi\ (2\rho)^3\ \sin^2\theta} . \quad (12)$$

In the above equation, a represents the area of an element of detection, $s(\theta)$ expresses any angular dependance of the γ-ray source distribution, and $P(\omega)$ (where $\omega = \pi/2+\varphi$) is the Klein-Nishina differential cross section. Mathematically, g is essentially the Radon transform of the object electron density $n_e(M)$ on arcs of circle, when radiation attenuation and photometric effects on radiation propagation are neglected.

Norton proposed an inverse formula given by:

$$n_e(r,\theta) = \frac{1}{\pi^2}\int_0^{2\pi} d\varphi \int_0^\infty d\rho\ \frac{g(\rho,\varphi)}{w(r,\theta;\rho,\varphi)} \times\ h\left[r - 2\rho\cos(\theta-\varphi)\right] \quad (13)$$

where

$$h(x) = \int_{-\infty}^{\infty} e^{-i\zeta x}\,|\zeta|\,d\zeta\ . \tag{14}$$

This expression is the same convolution kernel employed in the filtered Back-Projection algorithm used in x-ray transmission CT. The difference is that the Back-Projection is performed along straight lines in transmission CT, whereas here the Back-Projection is performed around the circles $r = 2\rho\ \cos(\theta - \varphi)$.

Now let :

$$\begin{cases} \mathcal{C}^1 f(\rho,\varphi) & = g(\rho,\varphi)\ \frac{(2\rho)^3}{P(\varphi)} \\ f(r,\theta) & = n_e(r,\theta)\ \frac{as(\theta)r}{4\pi\sin^2\theta} \\ p & = 2\rho \end{cases} \tag{15}$$

Substituting equation (15) in (11) we obtain:

$$\mathcal{C}^1 f(p,\varphi) = \int_0^{\pi} d\theta \int_0^{+\infty} dr\ p\ f(r,\theta)\ \delta\left\{r - p\cos(\theta-\varphi)\right\}\ . \tag{16}$$

From (16) we use the Fourier angular components of f and $\mathcal{C}^1 f$ (like previously) and we can show that :

$$\mathcal{C}^1 f_l(p) = 2\int_0^p dr\ f_l(r)\ \frac{\cos\left[|l|\cos^{-1}\left(\frac{r}{p}\right)\right]}{\sqrt{1-\left(\frac{r}{p}\right)^2}}\ dr\ . \tag{17}$$

Equation (17) is precisely the integral equation for f_l in the case of a ($\beta = 1$)-curve of Cormack [3, 4]. Thanks to a property between cos and cosh, he could derive the following inverse formula for this circular Radon transform

$$f_l(r) = \frac{1}{\pi r}\int_0^r \frac{\cosh(|l|\cosh^{-1}(\frac{r}{p}))}{\sqrt{(\frac{r}{p})^2-1}}\ \frac{d}{dp}\left[\mathcal{C}^1 f_l(p)\right] dp\ . \tag{18}$$

Finally $f(r,\theta)$ is reconstructed through its Fourier expansion with the circular harmonic components $f_l(r)$. We have thus established the forward and inverse transforms (eq. (17) and (18)) in the case of the Norton's Compton scattering tomography.

In the next section, we will discuss how to use these transforms for numerical image reconstruction and how to derive novel algorithms based on circular harmonic decomposition.

3. NUMERICAL INVERSIONS

In this part, we will work out the numerical inversions that we propose for the both Circular Radon transforms presented above.

3.1 Computation of inverse CART

In principle, one can use equation (10) to perform numerical computations. However, assuming that the original function is bounded, a close inspection of the integral kernel of equation (10) shows that it behaves as

$$\lim_{q\to+\infty} \frac{\cosh(|l|\ \cosh^{-1}(\frac{q}{t}))}{q\sqrt{(\frac{q}{t})^2-1}} \approx \lim_{u\to+\infty} 2\ e^{(|l|-2)u}\ , \tag{19}$$

where $u = \cosh^{-1}(\frac{q}{t})$. Equation (19) presents an apparent divergence when $|l| > 2$, since for $q \to \infty$ the integrand grows very rapidly. This explains that when $|l| > 2$, this apparent divergence makes the q-integral unstable, and as such the presence of noise in the data $\mathcal{C}^2 f_l(1/q)$ for large q is badly propagated into the calculation of $f_l(r)$ which prevents simulation studies. It becomes then obvious that equation (10) needs to be regularized.

Even if the circular arc doesn't belong to the α-curves family (defined by A.M. Cormack [3]), we will see that there is a frequential link between them. Indeed by introducing :

$$\begin{cases} F_l(t = \frac{2pr}{p^2-r^2}) = \frac{(p^2-r^2)^2}{2p(p^2+r^2)} \times f_l(r) \\ G_l(q) = \frac{\mathcal{C}^2 f_l(\frac{1}{q})}{\sqrt{1+q^2}}\ . \end{cases} \tag{20}$$

we obtain :

$$F_l(t) = (-)\frac{1}{\pi}\int_t^{\infty} dq\ \frac{\cosh(|l|\cosh^{-1}(q/t))}{\sqrt{q^2-t^2}}\ \frac{dG_l(q)}{dq}\bigg|_{t=\frac{2pr}{p^2-r^2}} \tag{21}$$

Equation (21) is precisely the straight-line Radon transform inversion formula ($\alpha = 1$) given by Cormack's regularization procedure. Thus with three changes of function, we pass from the original space of CART definition to a new space in which the CART becomes the ordinary Radon transform. Cormack proposed a regularization procedure based on consistency conditions of the circular harmonic components of the data

$$\int_0^{\infty} dq\ \frac{dG_l(q)}{dq}\ q^{\alpha_l} = 0 \quad \text{for} \quad \alpha_l = (l-1),(l-3),...,>0\ . \tag{22}$$

Thanks to these conditions and a property of the Tchebychev polynomial linking the polynomial of first kind ($T_l(.)$) to the second kind one ($U_l(.)$)

$$\frac{T_l(x)}{\sqrt{x^2-1}} = \frac{\left(x-\sqrt{x^2-1}\right)^l}{\sqrt{x^2-1}} + U_{l-1}(x)\ , \tag{23}$$

he could derive the following regularised inverse formula for the CART:

$$F_l(t) = \frac{1}{\pi t}\int_0^t dq\, G_l^{'}(q)\, U_{|l|-1}\left(\frac{q}{t}\right) - \frac{1}{\pi t}\int_t^{\infty} dq\, G_l^{'}(q)\, \frac{\left((q/t)-\sqrt{(q/t)^2-1}\right)^{|l|}}{\sqrt{(q/t)^2-1}}\ . \quad (24)$$

Then we follow the Chapman and Cary computional approach in the space where the Circular-Arc Radon transform becomes the standard Radon transform. In this algorithm we will consider that $(q,t) \in]0;Q]^2$ with the same sampling Δt and where $Q = \tan(\max\{\omega\})$. Now let $q = t\cos\chi$, (respectively $q = t\cosh\chi$) in the first (respectively the second) integral of equation (24). Thus :

$$F_l(t) = \frac{1}{\pi}\int_0^{\frac{\pi}{2}} d\chi\, G_l'(t\cos\chi)\, sin(l\chi) - \frac{1}{\pi}\int_0^{cosh^{-1}(Q/t)} d\chi\, G_l'(t\cosh\chi)\, e^{-l\chi} \quad (25)$$

Now we can define the discretized forms of $F_l(t)$ and $G_l(q)$ as :

$$\begin{cases} G_{lk} = G_l(k\Delta t) \\ F_{lj} = F_l(j\Delta t), \end{cases} \quad (26)$$

where $(j,k) \in [0,K]^2$ with $K = \frac{Q}{\Delta t}$. The derivative $G_l'(q)$ can be approximated by coefficients a_{lkm} where:

$$a_{lk} = \frac{G_{l(k+1)} - G_{lk}}{\Delta t}\ . \quad (27)$$

Equation (25) becomes so :

$$F_{lj} = \frac{1}{\pi}\left[\sum_{k=0}^{j-1} a_{lk}\left(I_l(\chi j(k+1)) - I_l(\chi jk)\right) + \sum_{k=j}^{K-1} a_{lk}\left(J_l(\chi j(k+1)) - J_l(\chi jk)\right)\right] \quad (28)$$

in terms of the primitive

$$I_l(\chi_{jk}) = \int^{\chi_{jk}} \sin(|l|x)dx = -\frac{\cos(|l|\chi_{jk})}{|l|} \quad \text{for} \quad l \neq 0 \quad (29)$$

and

$$J_l(\chi_{jk}) = \int^{\chi_{jk}} e^{-|l|x}dx = \begin{cases} -e^{-|l|\chi_{jk}}/|l| & \text{if } l \neq 0 \\ \chi_{jk} & \text{if } l = 0 \end{cases} \quad (30)$$

where

$$\chi_{jk} = \begin{cases} \cos^{-1}\left(\frac{k}{j}\right) & \text{for} \quad 0 \leq k \leq j \\ \cosh^{-1}\left(\frac{k}{j}\right) & \text{for} \quad j \leq k \leq K. \end{cases} \quad (31)$$

Finally the discretized form of the reconstruction equation appears as

$$F_{lj} = \frac{1}{|l|\pi}\sum_{k=0}^{j-1} a_{lk}\left(\cos|l|\chi_{j(k+1)} - \cos|l|\chi_{jk}\right) + \frac{1}{|l|\pi}\sum_{k=j}^{K-1} a_{lk}\left(e^{-|l|\chi_{j(k+1)}} - e^{-|l|\chi_{jk}}\right) \quad (32)$$

And for $l = 0$ a separate expression exists

$$F_{0j} = -\frac{1}{\pi}\sum_{k=j}^{K-1} a_{0k}\left(\chi_{j(k+1)} - \chi_{jk}\right). \quad (33)$$

So having obtained all the F_{lj}, which are the discretized circular components of the associated Radon transform, we recover the theoretical circular components of our circular-arc problem $f_l(r)$ by using formula (20) given by

$$f_l(r) = \frac{2p(p^2+r^2)}{(p^2-r^2)^2}\ F_l\left(\frac{2pr}{p^2-r^2}\right), \quad (34)$$

The final step consists in working out the summation in discrete form.

$$f(r,\theta) = \sum_l f_l(r)\ e^{il\theta}. \quad (35)$$

We have established an alternative algorithm of image reconstruction based on circular harmonic decomposition for this new Compton scattering tomography modality.

3.2 Computation of inverse CRT

To establish our numerical inversion in the case of the Circular Radon transform presented above, we start from its analytical inverse:

$$f_l(r) = \frac{1}{\pi r}\int_0^r \frac{\cosh(|l|\cosh^{-1}(\frac{r}{p}))}{\sqrt{(\frac{r}{p})^2-1}}\ \frac{d}{dp}\left[\mathcal{C}^1 f_l(p)\right] dp \quad (36)$$

This formula has the same kind of singularities that in the Circular-Arc Radon transform case since this transform belongs to the family of β-curves. So we can use the same method to regularize it and obtain :

$$f_l(r) = \frac{1}{\pi r}\int_0^r \frac{\left(\frac{r}{p} - \sqrt{(\frac{r}{p})^2 - 1}\right)^{|l|}}{\sqrt{(\frac{r}{p})^2 - 1}} \left(\mathcal{C}^1 f_l\right)'(p)dp - \frac{1}{\pi r}\int_r^{+\infty} U_{|l|-1}(r/p) \left(\mathcal{C}^1 f_l\right)'(p)dp \quad (37)$$

Then we will adapt the Chapman and Cary approach to this case. Indeed Chapman and Cary have studied the case of the ($\alpha = 1$)-curve and so the case of the standard Radon transform. Now from the same idea we will propose a computional approach to reconstruct the original function $f(r,\theta)$ from the data $\mathcal{C}^1 f(p,\varphi)$. As we cannot consider an infinite size, we shall define the maximum value of p, p_{max}, and a minimum value, p_{min}, because a scattering site cannot be the source. Since,

$$\cosh^{-1}(x) = \ln(x + \sqrt{x^2-1}) = -\ln(x - \sqrt{x^2-1}) \quad (38)$$

we obtain

$$f_l(r) = \frac{1}{\pi r}\int_{p_{min}}^r \frac{e^{-|l|\cosh^{-1}(r/p)}}{\sqrt{(\frac{r}{p})^2 - 1}} \left(\mathcal{C}^1 f_l\right)'(p)dp - \frac{1}{\pi r}\int_r^{p_{max}} U_{|l|-1}(r/p) \left(\mathcal{C}^1 f_l\right)'(p)dp \quad (39)$$

We make the change of variable $r = p\cosh(\chi)$ in the first integral and $r = p\cos(\chi)$ in the second one. The transform (39) becomes :

$$f_l(r) = \frac{1}{\pi}\int_0^{\cosh^{-1}\left(\frac{r}{p_{min}}\right)} \frac{e^{-|l|\chi}}{\cosh^2\chi} \left(\mathcal{C}^1 f_l\right)'\left(\frac{r}{\cosh\chi}\right)d\chi - \frac{1}{\pi}\int_0^{\cos^{-1}\left(\frac{r}{p_{max}}\right)} \frac{\sin(|l|\chi)}{\cos^2\chi} \left(\mathcal{C}^1 f_l\right)'\left(\frac{r}{\cos\chi}\right)d\chi \quad (40)$$

To simplify the algebra and notation we consider that p and r have the same sampling Δr. So we can define the discretized forms of $f_l(r)$ and $\mathcal{C}^1 f_l(p)$ as :

$$g_{lk} = \mathcal{C}^1 f_l(k\Delta r) \text{ and } f_{lj} = f_l(j\Delta r) \quad (41)$$

where $(j,k) \in [1,K]^2$ with $K = \frac{\Delta r}{p_{max}}$. Moreover we use linear interpolation to simplify the algorithm and the calculation of the derivative of the data g_l. So in the interval $k\Delta r < p < (k+1)\Delta r$, we can write:

$$\bar{g}_{lk} = \frac{g_{l(k+1)} - g_{lk}}{\Delta r} \ . \quad (42)$$

Finally we obtain a discretized form of our transform (eq (40))

$$f_{lj} = -\frac{1}{\pi}\left[\sum_{k=1}^{j-1} \bar{g}_{lk}\left(J_l(\chi_{j(k+1)}) - J_l(\chi_{jk})\right) + \sum_{k=j}^{K-1} \bar{g}_{lk}\left(I_l(\chi_{j(k+1)}) - I_l(\chi_{jk})\right)\right] \quad (43)$$

in terms of the primitive integrals :

$$I_l(\chi_{jk}) = \int^{\chi_{jk}} \frac{\sin(|l|x)}{\cos^2 x}dx \text{ and } J_l(\chi_{jk}) = \int^{\chi_{jk}} \frac{e^{-|l|x}}{\cosh^2 x}dx \ . \quad (44)$$

The variables χ_{jk} corresponds to the discrete radii $p = k\Delta r$

$$\chi_{jk} = \begin{cases} \cosh^{-1}\left(\frac{j}{k}\right) & \text{for} \quad 1 \le k \le j \\ \cos^{-1}\left(\frac{j}{k}\right) & \text{for} \quad j \le k \le K \end{cases} \quad (45)$$

We evaluate the primitive integrals (44) by recurrence :

$$I_n(x) = \frac{2}{n-2}\left(\tan x \sin((n-2)x) - \cos((n-2)x)\right) - \frac{n}{n-2}I_{n-2}(x) \quad (46)$$

with the initial conditions :

$$I_1(x) = \frac{1}{\cos x} \quad \text{and} \quad I_2(x) = -2\ln(\cos x) \quad (47)$$

In the same way, we make the change of variable $u = e^{\chi_{jk}}$ in the primitive and we let $n = |l| - 1$:

$$J_n(u) = \int \frac{du}{u^n\left(u^2+1\right)^2} \ . \quad (48)$$

So we obtain the following recurrence relation :

$$J_{n+1}(u) = -\frac{1}{nu^n\left(u^2+1\right)} - \frac{n+2}{n}J_{n-1}(u) \quad (49)$$

with the initial conditions :

$$J_0(u) = \frac{u}{2(u^2+1)} + \frac{1}{2}\arctan(u) \quad \text{and} \quad J_1(u) = -\frac{1}{2}\ln(u^2+1) + \ln(u) + \frac{1}{2(u^2+1)} \quad (50)$$

We have also the special case $l = 0$. In this case, we evaluate the primitive integral $J_0(\chi_{jk})$

$$J_0(\chi_{jk}) = \int^{\chi_{jk}} \frac{1}{\cosh^2 x} dx = \frac{\sinh \chi_{jk}}{\cosh \chi_{jk}} = \sqrt{1 - \left(\frac{k}{j}\right)^2} \tag{51}$$

hence,

$$f_{0j} = -\frac{1}{\pi} \sum_{k=1}^{j-1} \bar{g}_{0k} \left(\sqrt{1 - \left(\frac{k+1}{j}\right)^2} - \sqrt{1 - \left(\frac{k}{j}\right)^2} \right) . \tag{52}$$

So having obtained all the f_{lj}, which are the discretized circular components of our circular problem by constructing the theoretical $f_l(r)$. Finally we work out the summation in discrete form to obtain the original function.

$$f(r, \theta) = \sum_l f_l(r)\ e^{il\theta}. \tag{53}$$

We have established an alternative algorithm of image reconstruction based on circular harmonic decomposition for the Norton's Compton scattering tomography. Moreover this algorithm is an alternative to which proposed Norton.

In the last section, we present the numerical results in order to prove the efficiency of our algorithms.

4. SIMULATION RESULTS

In this section, we present the numerical simulations of both circular Radon transforms (CART-CHD and CRT-CHD) and compare the reconstructions obtained by the ordinary Radon transform filtered back-projection (RT FBP) in the case of $\mathcal{C}^2$ and by the Norton's inverse formula, which can be apparented to a "filtered back-projection" on circles (NRT FBP), in the case of $\mathcal{C}^1$.

Moreover the main aim of this work is to establish a new imaging principle by Compton scattered radiation. This is why other factors in realistic imaging systems are not treated here such as medium attenuation, inhomogeneous electron density and Poisson emission noise.

To illustrate and compare the quality of the reconstructions, we define the normalized mean square error ($NMSE$) and the normalized mean absolute error($NMAE$):

$$NMSE = \frac{\|I_r - I_o\|_2^2}{N^2}, \tag{54}$$

$$NMAE = \frac{\|I_r - I_o\|_1}{N^2}, \tag{55}$$

where I_r is the reconstructed image, I_o is the original image (ground truth) and N^2 is the size of the studied image.

4.1 Image reconstructions by CART-CHD and RT-FBP

As an illstration of the feasibility of our new algorithm, we present numerical simulations applied on the medical phantom (Fig. 3). The scattering medium is discretized with 512×512 of length units (pixels). We consider the number of rotational positions N_φ and the number of energy levels N_ω. These numbers define the corresponding angular sampling steps $d\varphi$ and $d\omega$ by :

$$d\varphi = \frac{2\,\pi}{N_\varphi} \quad \text{and} \quad d\omega = \frac{\pi}{2N_\omega}. \tag{56}$$

In order to have a "well-conditioned" problem, the number of projections ($N_\varphi \times N_\omega$) must be larger than the number of image pixels (512×512). This is why we take $N_\varphi = 720$ and $N_\omega = 500$. Moreover we take the constant term $p = 512$ and $\min\{\omega\} = d\omega$.

Let us recall the classical Radon transform which is defined as integral of object function on straight lines. The forward Radon transform is:

$$g(u, \varphi) = \int_{\mathbb{R}^2} dxdy\ f(x, y)\ \delta\left(u - x\cos\varphi - y\sin\varphi\right), \tag{57}$$

and its inverse transform is:

$$\begin{aligned} f(x,y) &= \int_0^\pi d\varphi \int_{-\infty}^{+\infty} du \int_{-\infty}^{+\infty} d\nu\ |\nu| \times \\ &\quad e^{-2i\pi\nu(u - x\cos\varphi - y\sin\varphi)} g(u,\varphi) \\ &= -\frac{1}{2\pi^2} \int_0^\pi d\varphi \left\{ P.V. \int_{-\infty}^{+\infty} du\ \frac{\partial g(u,\varphi)}{\partial u} \right. \\ &\quad \left. \frac{1}{u - x\cos\varphi - y\sin\varphi} \right\} . \end{aligned} \tag{58}$$

Equation (58) is called the filtered backprojection method (FBP). In this case, FBP is an exact inversion formula obtained by combining the action of the ramp filter ($|\nu|$)and the backprojection operation of the Radon transform. This is the most popular inversion method for the ordinary Radon transform owing to its rapid algorithmic implementation.

The CART-CHD approach gives in general a reasonable image quality in the reconstruction of the medical phantom (Fig. 8). Indeed, contours and small structures are well recovered. Moreover, we can observe that there are a lot fewer artifacts compared to FBP reconstruction (Fig. 7) around the studied object. This is due to the fact that the CART-CHD reconstruction is consistent with the Radon data. The numerical error measurements (Table 1) obtained using the CART-CHD are very close to those of the ordinary Radon transform and proves the feasibility and the interest of this algorithm.

4.2 Image reconstructions by CRT-CHD and by NRT-FBP

Now we will present the numerical simulations in the case of our algorithm of the circular Radon transform applied on the Shepp-Logan phantom (Fig. 4). But this case we put the phantom farther from the source in order to avoid artifacts generated by the $1/r$ factor. Moreover the source is placed below on the left of the image and the detector moves along the axis Sx. The scattering medium is discretized with 256×256 of length units (pixels). We consider the number of rotational positions N_φ and the number of radii N_p. These numbers define the corresponding sampling steps $d\varphi$ and dp by :

$$d\varphi = \frac{2\,\pi}{N_\varphi} \quad \text{and} \quad dp = \frac{4 * 256}{N_p}. \tag{59}$$

We take $N_\varphi = N_p = 4 * 256$. As the system of the corresponding CST is to not rotate around the object, the (φ, p)-space is very large in front of the studied image. So to "well-observe" the object we have to take a large maximum value of p (4 times the image size).

The CRT-CHD approach gives a very interesting image quality in the reconstruction of the Shepp-Logan phantom (Fig. 11). Indeed, contours and small structures are better recovered than with the Norton's inverse formula (Fig. 10). Nevertheless we have more artifacts generated around the studied object than in the Norton's case. This is due to the fact that the $p \in \mathbb{R}^+$ and that we have to fix a maximum value p_{max}. Therefore this loss of information generated artifacts. To reduce this artifacts, we have to increase p_{max} and so to increase the length of the detector in the related CST. The numerical error measurements (Table 1) obtained using the CRT-CHD are smaller as compared to those of the Norton's inverse formula and prove the feasibility of this algorithm, particularly in the domain of the non-destructive testing.

Method		$NMAE$	$NMSE$
RT-FBP	Fig. 7	0.0056	8×10^{-6}
CART-CHD	Fig. 8	0.006	2.8×10^{-5}
NRT-FBP	Fig. 10	0.029	7.48×10^{-4}
CRT-CHD	Fig. 11	0.028	5.9×10^{-4}

Table 1: "NMSE and NMAE for various reconstructions of the medical phantoms (Figs. 3 and 4)"

5. CONCLUSION

Alternative algorithms for the numerical inversion of two circular Radon transforms are established. Based on the circular harmonic decomposition, the advantage of these algorithms is to produce consistent image with the data (forward transforms) as opposed to analytical conventional methods like the "filtered back-projection" algorithm and to have the same computational complexity than the "filtered back-projection" method.

In the circular-arc Radon transform case, the simulation results prove the feasibility of the associated Compton scattering tomography which is suitable for biomedical imaging or non-destructive testing for example and could present an alternative to X-ray tomography. In the second case we have compared our algorithm to the Norton's inverse formula. Even if it seems hard to choose the best reconstruction way, we can say that both approaches are complementary since Norton's method gives a general reconstruction whereas ours reconstructs with more details of the small structures and the boundaries. The associated Compton scattering tomography is more suitable for the industrial nondestructive evaluation since we can reconstruct the original medium from one side of the object and without rotation.

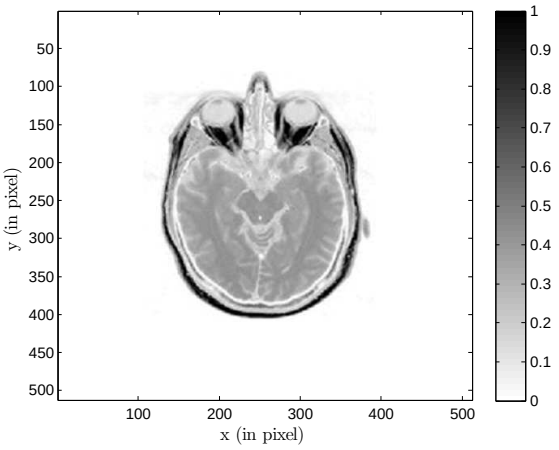

Figure 3: Illustration of a medical phantom.

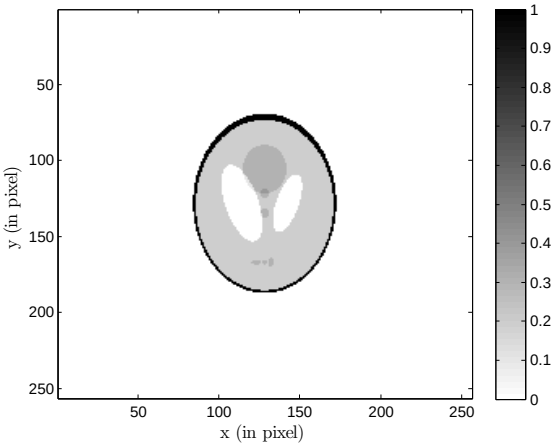

Figure 4: Illustration of the Shepp-Logan phantom of size 128×128**.**

6. REFERENCES

[1] J. Radon, "Uber die bestimmung von funktionnen durch ihre integralwerte längs gewisser mannigfaltikeiten," *Ber. Verh. Sachs. Akad. Wiss. Leipzig-Math. Natur. Kl.*, vol. 69, pp. 262–277, 1917.

[2] E. T. Quinto, "Radon transforms of curves in the

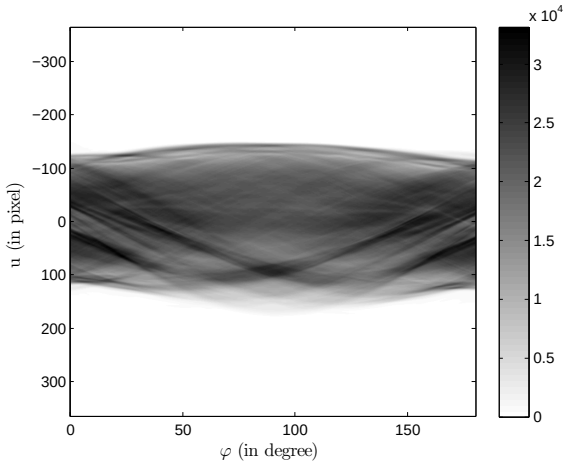

Figure 5: Radon transform of the medical phantom shown in figure 3

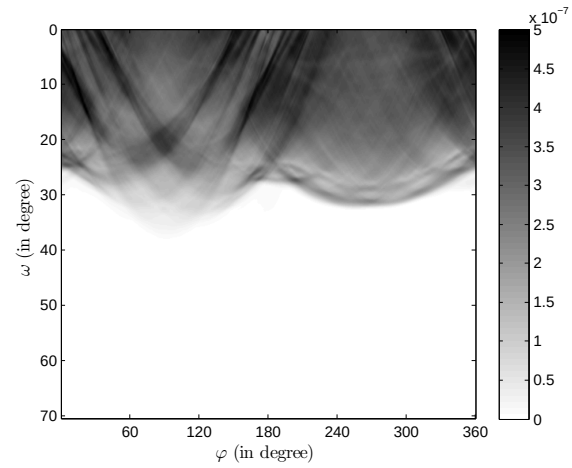

Figure 6: CART of the medical phantom shown in figure 3

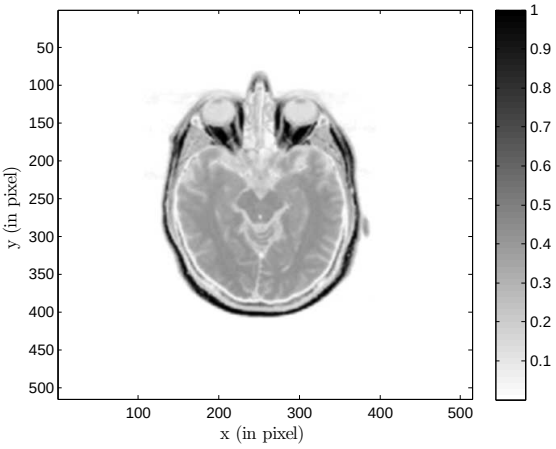

Figure 7: Reconstruction of the medical phantom shown in figure 3 using RT-FBP and data in figure 5.

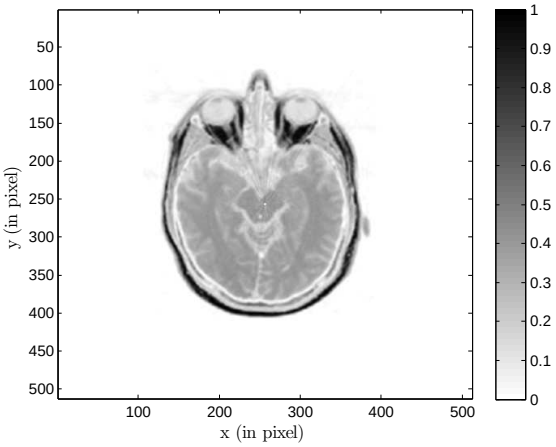

Figure 8: Reconstruction of the medical phantom shown in figure 3 using CART-CHD and data in figure 6.

plane," *Lectures in Applied Mathematics : Tomography, Impedance Imaging and Integral Geometry*, vol. 30, pp. 231–244, 1994.

[3] A. M. Cormack, "The Radon transform on a family of curves in the plane," *Proceedings of the American Mathematical Society*, vol. 83, pp. 325–330, October 1981.

[4] A. M. Cormack, "Radon's problem - old and new," *SIAM-AMS Proceedings*, vol. 14, pp. 33–39, 1984.

[5] C. H. Chapman and P. W. Cary, "The circular harmonic Radon transform," *Inverse Problems*, vol. 2, pp. 23–49, 1986.

[6] S. J. Norton, "Compton scattering tomography," *Jour. Appl. Phys.*, vol. 76, pp. 2007–2015, 1994.

[7] M. K. Nguyen and T. T. Truong, "Inversion of a new circular-arc Radon transform for Compton tomography," *Inverse Problems*, vol. 26, 065005 (13 pp), 2010.

[8] M. K. Nguyen and T. T. Truong, "On an integral transform and its inverse in nuclear imaging," *Inverse Problems*, vol. 18, pp. 265–277, 2002.

[9] M. K. Nguyen, T. T. Truong, H. D. Bui and J. L. Delarbre , "A novel inverse problem in gamma-ray emission imaging," *Journal of Inverse Problems in Science and Engineering*, vol. 12, pp. 225–246, 2004.

[10] M. K. Nguyen, T. T. Truong, J. L. Delarbre, Ch. Roux and H. Zaidi, "Novel approach to stationary transmission scanning using Compton scattered radiation," *Physics in Medicine and Biology*, vol. 52, pp. 4615–4632, 2007.

[11] M. K. Nguyen, T. T. Truong, C. Driol and H. Zaidi, "On a novel approach to Compton scattered emission imaging," *IEEE Transactions on Nuclear Science*, vol. 56, pp. 1430–1438, June 2009.

[12] D. A. Meneley, E. M. A. Hussein and S. Banerjee, "On the solution of the inverse problem of radiation scattering imaging," *Nuclear Science and Engineering*, vol. 92, pp. 341–349, 1986.

[13] N. V. Arendtsz and E. M. A. Hussein, "Energy-spectral Compton scatter imaging - part 1: theory and mathematics," *IEEE Transactions on Nuclear Sciences*, vol. 42, pp. 2155–2165, 1995.

[14] R. Guzzardi and G. Licitra, "A critical review of Compton imaging," *CRC Critical Reviews in Biomedical Imaging*, vol. 15, pp. 237–268, 1988.

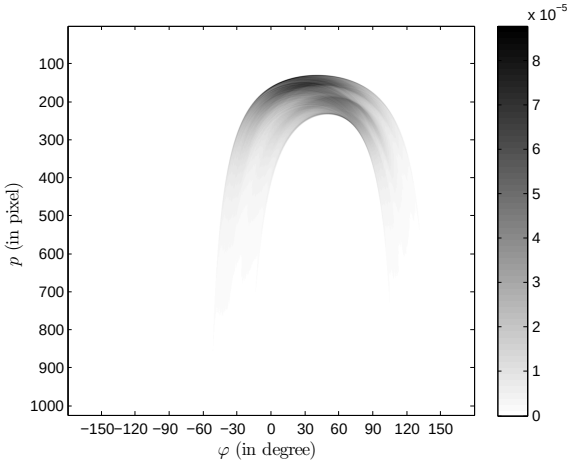

Figure 9: CRT of the Shepp-Logan phantom shown in figure 4

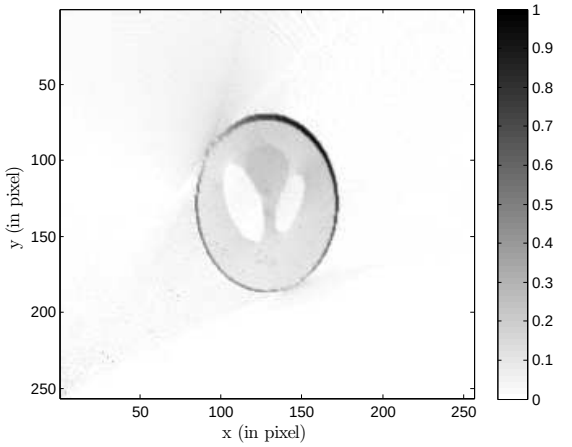

Figure 10: Reconstruction of the Shepp-Logan phantom shown in figure 4 using NRT-CHD and data in figure 9.

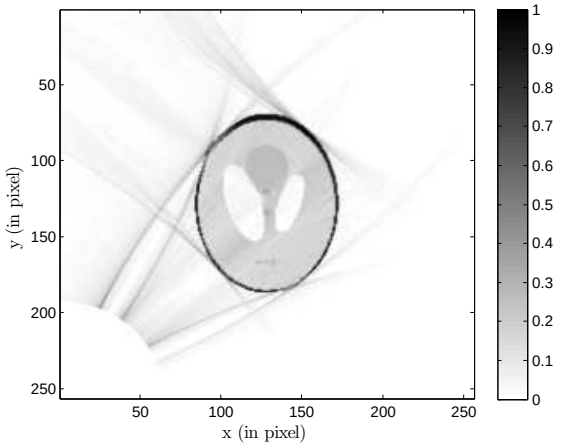

Figure 11: Reconstruction of the Shepp-Logan phantom shown in figure 4 using CRT-CHD and data in figure 9.